



The continuous generating grinding method for face gears based on general cylindrical gear grinding machine

Kun He^{1,3} · Xiaohu He¹ · Guolong Li² · Aoting Wang¹ · Quanfu Ran² · Shilong Wang²

Received: 23 September 2022 / Accepted: 22 January 2023 / Published online: 4 February 2023
© The Author(s), under exclusive licence to Springer-Verlag London Ltd., part of Springer Nature 2023

Abstract

This study achieves precision grinding of face gears in the general cylindrical gear grinding machine, meeting the increasing demand for efficiency and accuracy in face gear manufacturing. The machining motion of face gears is more complex than that of cylindrical gears, and the general gear grinding machine cannot meet the motion of continuous generating grinding of face gears. The worm forming dressing method based on virtual center distance is proposed to replace diamond wheel deflection with worm deflection, to solve that the diamond wheel cannot be deflected when dressing the crown worm wheel. The radial feed trajectory for grinding face gears is replanned to replace the linear feed with diagonal feed, to solve that the crown worm wheel cannot deflection horizontal during face gear grinding. Finally, the tooth surface errors caused by the misalignment of the crown worm wheel during grinding are analyzed, and the numerical simulation and machining experiments are conducted for worm dressing and face gear grinding. The results show that the shape of the dressed worm is consistent with the simulation results, and the deviation of the machined face gear is within the error range of grade 5 accuracy.

Keywords Face gears · Continuous generating grinding · Crown worm wheel dressing · General gear grinding machine

1 Introduction

The face gear is a new type of staggered shaft drive gear applied in the aviation field, which has the advantages of a stable transmission ratio, high overlap, and a simple support structure [1]. Face gears used in helicopter power units can make the reducer more compact and torque splitting accuracy and gradually replace bevel gears as the core component of helicopter drive systems [2, 3].

Face gear grinding can significantly improve the machining accuracy and surface quality of tooth surfaces. The main processing methods are disc grinding and worm grinding [4]. In the field of disc wheel grinding research, Tang et al. [5] proposed a plan for grinding a modified face gear using a

disc wheel, derived the equations for the modified face gear and the corresponding disc wheel tooth surface, calculated the range of swing angles for the entire tooth surface of the disc wheel ground face gear, and verified the correctness of the proposed method by Vericut machining simulation. Guo et al. [6–8] proposed a grinding plan for face gear manufactured by a disk wheel, investigated the envelope residuals of disc wheel grinding of face gears based on a five-coordinate machine tool, and proposed an optimization method to reduce tooth surface deviation. Wang et al. [9–11] analyzed the face gear drive principle, designed the disc wheel shape, developed a unique machine tool, proposed a motion control method for grinding face gears with disc wheels, established a mathematical model for roughness based on disc wheels, and studied the face gear generation grinding method using CBN wheels.

In the field of worm wheel grinding research, Litvin et al. [12, 13] proposed an analytical method for determining the worm thread surface, avoiding singularities and worm dressing, developed a computer program for generating face gears by grinding worm shafts, and proposed a new method for grinding face gears with specially shaped worm shafts. Tang et al. [14–17] suggested a multistep process for grinding face gears with worm gears when the working part of the gear tooth surface is not entirely covered. The worm wheel mounting

✉ Kun He
hekun@ctbu.edu.cn

¹ Chongqing Key Laboratory of Manufacturing Equipment Mechanism Design and Control, Chongqing Technology and Business University, Chongqing 400067, China

² State Key Laboratory of Mechanical Transmissions, Chongqing University, Chongqing 400044, China

³ Chongqing Machine Tool (Group) Co., Ltd, Chongqing 400055, China

error was analyzed, and the face gear grinding processing tooth surface error was studied and compared with the Vericut simulation. In addition, the method of changing the diamond wheel profile and modifying the face gear was proposed and verified by simulation. An accurate measurement method is proposed to obtain a tooth surface model for digital tooth contact analysis [18], and it is further applied in accurate and intelligent machining [19, 20]. Guo et al. [21] established a nonlinear contact equation for dressing grinding worm with standard double cone dressing and proposed an approximate method of grinding worm surface with variable meshing angle for grinding face gears. The continuous grinding process of the worm wheel can make each tooth surface of the face gear with high consistency, and has better tooth pitch control than the disc wheel spreading grinding tooth by tooth.

In addition to disc grinding and worm wheel grinding, some scholars have also studied other face gear processing methods. Tang et al. [22] proposed a method for planning spur face gears on a four-axis CNC planer. Guo et al. [23, 24] proposed a method for machining face gears with a circular cutter with a tool profile tilt angle. Chu et al. [25] offered a new way for grinding face gears along the contact trace using a disc CBN wheel. Zschippang et al. [26] described a general method for face gear with helix angle, axial angle, and axial offset of the tooth face generative approach. Wang et al. [27] proposed a shaving method for face gears. Zhang et al. [28] proposed a new way of tooth grinding based on continuous indexing, which uses a conical grinding tool to replace the blade on the face-hobbing cutter head. Yang et al. [29] proposed a face gear plunge milling method. However, these new machining methods are all in the theoretical research stage due to machine tools and equipment limitations.

All the above methods can realize the machining of face gears. However, with the increasing requirements of the application environment of face gears, the machining process is still dominated by worm grinding, and worm grinding can process face gear with high precision. In addition, worm grinding has high processing efficiency due to the principle of continuous generation. At present, some research institutions have carried out the development of face gear grinding machines. However, it is still in the laboratory prototype stage, and it is a special machine for face gears, which is not very versatile, and the maximum deviation of the face gear grinding measurement results is $52.6 \mu\text{m}$ [25].

A method for continuous generation grinding of face gears on a general cylindrical gear grinding machine is investigated to achieve precision generation grinding of face gears. The topology of the grinding machine and the dressing motion characteristics of the crown worm wheel are analyzed, and a forming dressing method based on the virtual center distance

principle is proposed. The motion principle of grinding the face gear by the crown worm wheel is analyzed, and the motion trajectory of face gear grinding is replanned. The tooth surface errors caused by worm misalignment during grinding are analyzed, and the face gear grinding function is realized without affecting the ordinary cylindrical gear grinding process, which is of great significance for improving the versatility of gear machine tools and the development of face gear precision grinding processing technology.

2 Problem description

Due to the limitations of the machine structure, the large deflection of the diamond wheel cannot be achieved during the worm dressing motion when machining the face gear on a general cylindrical gear grinding machine, and the horizontal deflection of the worm cannot be achieved when the grinding of face gears. The dressing structure of the general cylindrical gear grinding machine is shown in Fig. 1. The main motion axes are radial slide X1, wheel axis slide Y1, vertical stroke slide Z1, wheel swivel axis A1, cutter spindle B1, and workpiece spindle C1, which can realize six axes linkage. Besides, there are dressing spindle B2 and roller swivel axis C2.

The movements of X1, Z1, A1, and B2 are independent, and only the linkage coupling exists between B1 and Y1 when dressing a cylindrical worm wheel on the grinding machine. In comparison, the dressing motion of the crown worm wheel requires not only the axial translation of the worm but also the circumferential deflecting motion of the diamond wheel. The deflected diamond wheel dresses both sides of the crown worm wheel, which changes the cone angle of the diamond wheel and increases the dressing range of the diamond wheel. The diamond wheel deflection motion cannot be realized on the machine tool during the crown worm wheel forming dressing. Consider the method to realize the forming dressing of the crown worm wheel without changing the topological relationship of each axis of the machine tool.

The normal section profile of the worm wheel is the same as the end face profile of the shaper cutter. Figure 2 shows the shaper cutter on the left side of the face gear, with the two axes perpendicular to each other. The worm wheel deflects the spiral angle λ_w to ensure that the normal section participates in the enveloping process. The worm wheel constantly rotates with the face gear, and the worm wheel radial feeds along the face gear, where the speed relationship between the worm wheel and the gear is shown in Eq. (1).

$$\frac{n_2}{n_w} = m_{2w} = \frac{N_w}{N_2} \quad (1)$$

Fig. 1 The structure of the general cylindrical gear grinding machine

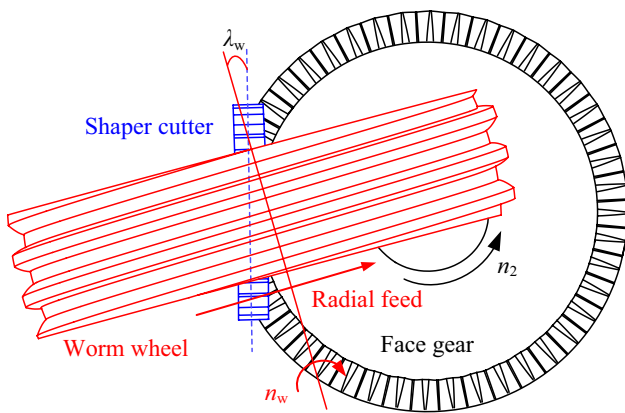
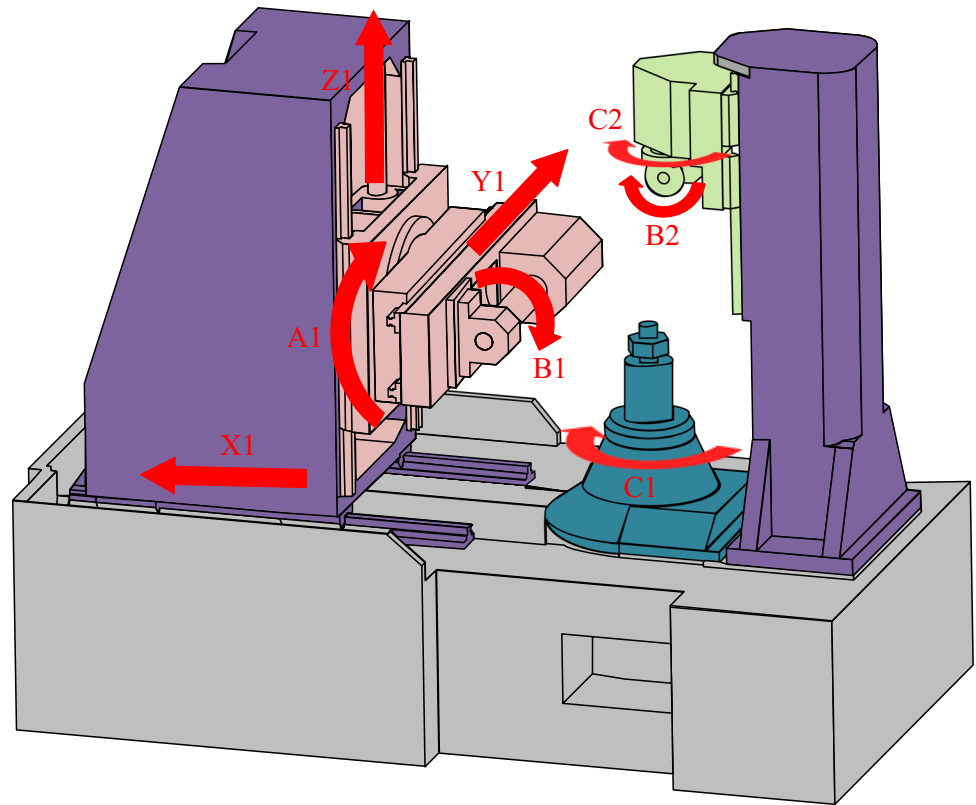


Fig. 2 Worm wheel grinding motion

where n_2 and n_w are the face gear and worm wheel speed, m_{2w} is the transmission ratio, N_2 and N_w are the teeth number of the face gear and the head number of the worm wheel.

The teeth of the face gear are distributed on the end face, the grinding stroke is completed by radial feed, and the grinding depth is changed by axial feed. The worm wheel needs to be deflected in the horizontal plane when it is radial feed in the direction shown in Fig. 2. According to

the grinding machine structure shown in Fig. 1, the worm movement cannot be realized on the machine tool. To avoid additional machine axes, the grinding trajectory of the crown worm wheel must be redesigned to fit the current machine axis layout.

3 Forming dressing method of the crown worm wheel

3.1 Tooth surface of face gears

The meshing of a face gear drive is shown in Fig. 3. The face gear and the conjugate pinion mesh between two non-parallel shafts. The meshing process is simulated as the generation process of face gear, where the shaper cutter replaces the cylindrical gear [30].

The machining coordinate system of face gear is established as shown in Fig. 3. S_m is the fixed coordinate system on the shaper cutter, S_s is the moving coordinate system of the shaper cutter, S_p is the fixed coordinate system on the face gear, and S_2 is the moving coordinate system of the face gear. The coordinate system of the shaper cutter is established at a position coincident with the origin of the face gear coordinate system. ϕ_s and ϕ_2 are the rotation angles of the shaper cutter and the face gear.

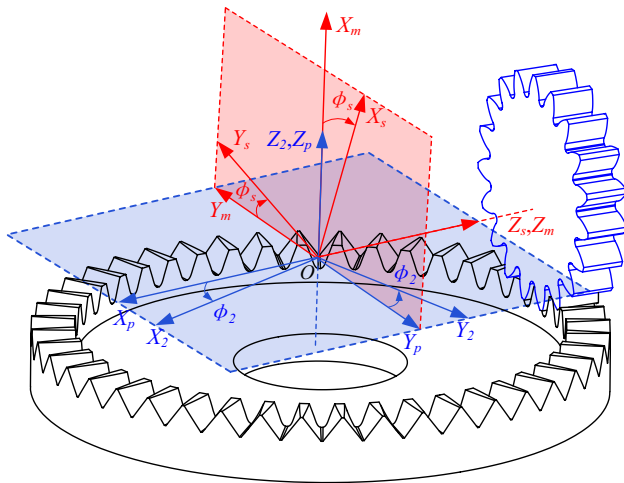


Fig. 3 The machining coordinate system of face gear

$$\phi_2 = m_{2s}\phi_s = \frac{N_s}{N_2}\phi_s \tag{2}$$

where m_{2s} is the transmission ratio, and N_s and N_2 are the teeth number of the shaper cutter and the face gear.

The transformation matrix from the S_s to the S_2 as

$$M_{2s}(\phi_s) = M_{2p}M_{pm}M_{ms} = \begin{bmatrix} \cos\phi_2\sin\phi_s & -\cos\phi_2\cos\phi_s & \sin\phi_2 & 0 \\ \sin\phi_2\sin\phi_s & -\sin\phi_2\cos\phi_s & -\cos\phi_2 & 0 \\ \cos\phi_s & \sin\phi_s & 0 & 0 \\ 0 & 0 & 0 & 1 \end{bmatrix} \tag{3}$$

The shaper cutter is a standard involute gear as shown in Fig. 4. The tooth surface can be represented as [31]

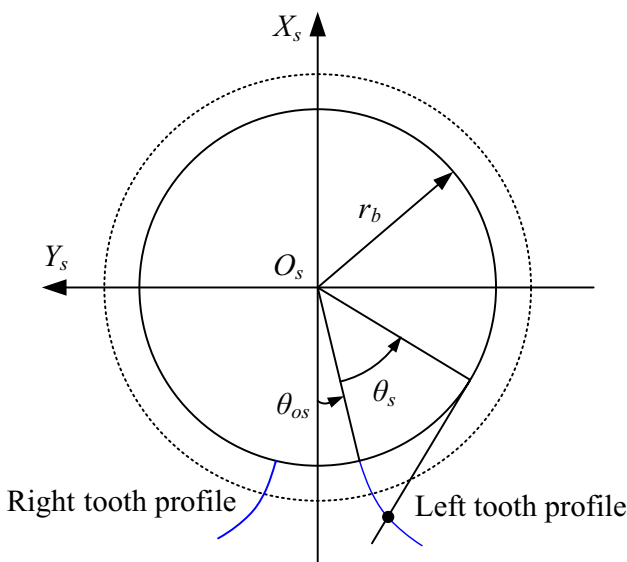


Fig. 4 The involute tooth profile of the shaper cutter

$$\vec{r}_s(\theta_s, u_s) = \begin{bmatrix} x_s \\ y_s \\ z_s \\ 1 \end{bmatrix} = \begin{bmatrix} -r_b[\cos(\theta_{os} + \theta_s) + \theta_s\sin(\theta_{os} + \theta_s)] \\ \pm r_b[\sin(\theta_{os} + \theta_s) - \theta_s\cos(\theta_{os} + \theta_s)] \\ u_s \\ 1 \end{bmatrix} \tag{4}$$

where r_b is the base circle radius of the shaper cutter, θ_s is the involute angle parameter, u_s is the parameter of the tooth width direction, ‘+’ is the right tooth shape, ‘-’ is the left tooth shape, θ_{os} is the half angle of the tooth groove.

$$\theta_{os} = \frac{\pi}{2N_s} - \text{inv}\alpha_0 \tag{5}$$

where α_0 is the pressure angle of the indexing circle.

The working part and the fillet part of the face gear are shown in Fig. 5. The working part participates in the meshing in the transmission, which is the central part. According to the principle of tooth surface enveloping, the tooth surface of the face gear is shown in Eq. (6).

$$\begin{cases} \vec{r}_2(u_s, \theta_s, \phi_s) = M_{2s}(\phi_s)\vec{r}_s(\theta_s, u_s) \\ f(u_s, \theta_s, \phi_s) = \vec{n}_s \cdot \vec{v}_{s2} = 0 \end{cases} \tag{6}$$

where $\vec{r}_2(u_s, \theta_s, \phi_s)$ is the tooth surface equation of the face gear, $f(u_s, \theta_s, \phi_s)$ is the meshing equation, \vec{n}_s is the normal line of the shaper cutter, and \vec{v}_{s2} is the relative velocity of the meshing point [31].

$$\vec{r}_2(\theta_s, \phi_s) = \begin{bmatrix} x_2 \\ y_2 \\ z_2 \\ 1 \end{bmatrix} = \begin{bmatrix} -r_b[\sin\phi_2(\sin\phi_\theta - \theta_s\cos\phi_\theta) + \frac{\cos\phi_2}{m_{2s}\cos\phi_\theta}] \\ \pm r_b[\cos\phi_2(\sin\phi_\theta - \theta_s\cos\phi_\theta) - \frac{\sin\phi_2}{m_{2s}\cos\phi_\theta}] \\ -r_b(\cos\phi_\theta + \theta_s\sin\phi_\theta) \\ 1 \end{bmatrix} \tag{7}$$

where $\phi_\theta = \phi_s + \theta_{os} + \theta_s$, and $\phi_2 = m_{2s}\phi_s$.

The fillet part is at the inside tooth root of the face gear, and there is a common line of intersection between it and the working part. The fillet part is formed by the edge envelope of the shaper cutter top and does not participate in the meshing contact. The fillet part in the S_2 is shown in Eq. (8) [31].

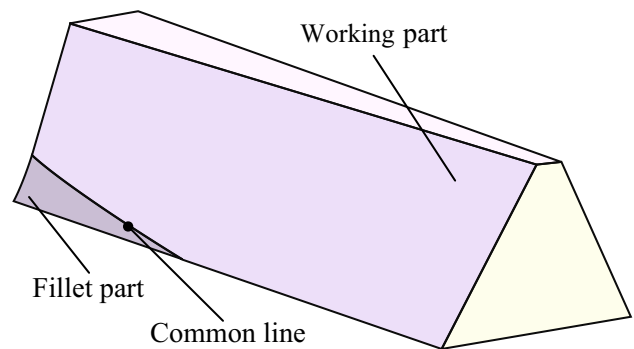


Fig. 5 Face gear tooth surface

$$\vec{r}_2^*(u_s, \phi_s) = M_{2s}(\phi_s)\vec{r}_s^*(u_s, \theta_s^*) \tag{8}$$

The fillet part can be obtained by giving different values of u_s and ϕ_s, θ_s^* is the involute parameter of the shaper cutter tooth top.

3.2 Crown worm wheel profile

The profile calculation of the worm is based on the conjugate surface envelope theory, and the worm profile is calculated by solving the meshing equation. The worm profile is formed by the single parameter envelope of the shaper cutter. Figure 6 shows the shaper cutter and the crown worm gear in a hypothetical internal mesh. The coordinate system S_{m1} is the fixed coordinate system on the shaper cutter, S_{s1} is the moving coordinate system of the shaper

cutter, S_a is the fixed coordinate system on the worm wheel, S_{w1} is the crown worm wheel motion coordinate system, and S_{n1} is the auxiliary coordinate system. E_{ws} is the shortest distance between the crown worm wheel's and shaper cutter's axes. λ_w is the spiral angle of the crown worm wheel. ϕ_s and ϕ_w are the rotation angles of the shaper cutter and the crown worm wheel.

$$\phi_w = m_{ws}\phi_s = \frac{N_s}{N_w}\phi_s \tag{9}$$

where m_{ws} is the transmission ratio of the shaper cutter to the crown worm wheel.

The transformation matrix from the S_{s1} to the S_{w1} is shown in Eq. (10).

$$M_{w1s1}(\phi_s) = M_{w1a}M_{an1}M_{n1m1}M_{m1s1}$$

$$= \begin{bmatrix} -\cos\phi_s\sin\phi_w + \sin\lambda_w\sin\phi_s\cos\phi_w & -\sin\phi_s\sin\phi_w - \sin\lambda_w\cos\phi_s\cos\phi_w & \cos\lambda_w\cos\phi_w & E_{ws}\sin\phi_w \\ \cos\phi_s\cos\phi_w + \sin\phi_s\cos\phi_w - \sin\lambda_w\sin\phi_s\sin\phi_w & \sin\phi_s\cos\phi_w - \sin\lambda_w\cos\phi_s\sin\phi_w & \cos\lambda_w\sin\phi_w & -E_{ws}\cos\phi_w \\ \sin\lambda_w\sin\phi_s\sin\phi_w & \sin\lambda_w\cos\phi_s\sin\phi_w & -\cos\lambda_w\sin\phi_s & \sin\lambda_w \cdot 0 \\ -\cos\lambda_w\sin\phi_s & \cos\lambda_w\cos\phi_s & \sin\lambda_w & 0 \\ 0 & 0 & 0 & 1 \end{bmatrix} \tag{10}$$

According to the conjugate envelope principle, the crown worm wheel profile \vec{r}_{w1} in the S_{w1} is shown in Eq. (11).

$$\begin{cases} \vec{r}_{w1}(\phi_s, \theta_s, u_s) = M_{w1s1}(\phi_s)\vec{r}_{s1}(\theta_s, u_s) \\ f_{ws}(\phi_s, \theta_s, u_s) = \vec{n}_s \cdot \vec{v}_s^{sw} = 0 \end{cases} \tag{11}$$

where $\vec{r}_{w1}(\phi_s, \theta_s, u_s)$ is the surface equation of the crown worm wheel, $f_{ws}(\phi_s, \theta_s, u_s)$ is the meshing equation, \vec{n}_s is the normal unit vector of the shaper cutter tooth surface, and \vec{v}_s^{sw} is the relative velocity. The crown worm wheel profile is shown in Eq. (12).

$$\vec{r}_{w1}(\theta_s, \phi_s) = \vec{r}_{w1}(\phi_s, \theta_s, u_s(\phi_s, \theta_s)) \tag{12}$$

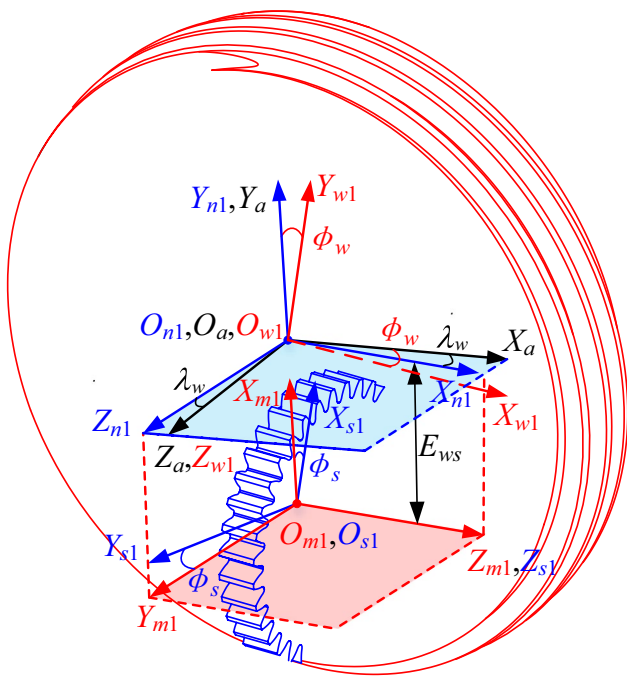


Fig. 6 Coordinate systems of the shaper cutter mesh with the crown worm wheel

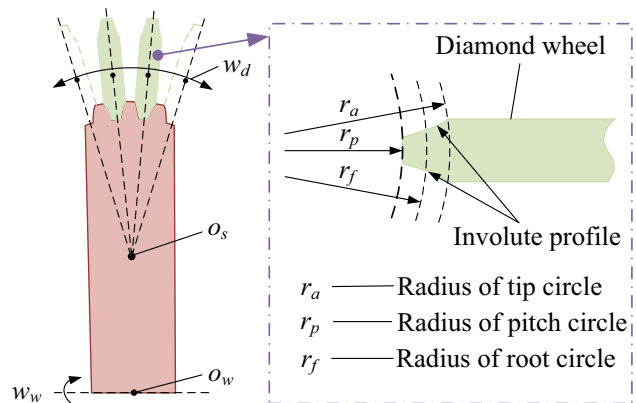


Fig. 7 Crown worm wheel dressing motion

3.3 Forming dressing method

The profile calculation of the crown worm wheel is based on the conjugate surface envelope theory, which is formed by the shaper cutter enveloped by a single parameter. Figure 7 shows that the profile of the shaft section of the design diamond wheel is consistent with the profile of the normal section of the crown

worm wheel. The diamond wheel makes a spirally sweeping motion and maintains linear contact with the normal section of the crown worm wheel. The crown worm wheel rotates, and the eccentric deflection motion with eccentric O_s as the center is the dressing stroke motion. The eccentric O_s does not necessarily coincide with the wheel center O_w . The relationship between the speed of eccentric deflection motion n_d and the rate of crown worm wheel rotation n_w is shown in Eq. (13).

$$\frac{n_d}{n_w} = \frac{1}{m_{ws}} = \frac{N_w}{N_s} \tag{13}$$

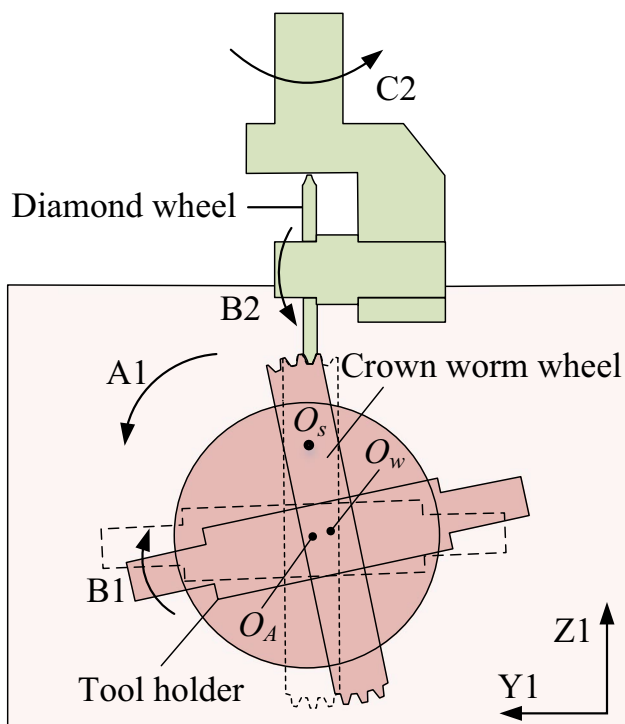
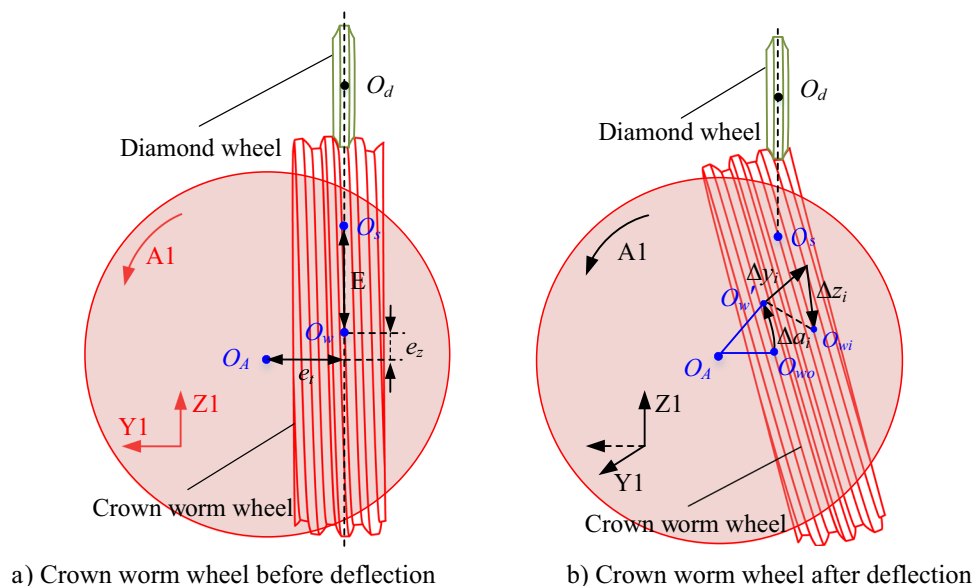


Fig. 8 Crown worm wheel dressing method based on virtual center distance

The deflection of the diamond wheel completes the dressing process instead of the deflection of the crowned worm wheel. This method avoids changing the topology of each axis of the machine and not adding the linkage axis. Figure 8 shows the crown worm wheel’s deflection motion with the eccentric O_s as the center. This motion cannot be realized through the movement of a single axis. The principle of virtual center distance machining [32] regards any plane motion in the machining process as a combination of translational and rotational around the base point. The eccentric deflection motion of the crown worm wheel is decomposed into two movements based on the virtual center distance machining principle. One is the rotation of the crown worm wheel around the center O_A , which the A1 realizes. The other is the translation of the crown worm wheel in the Y–Z plane, which is recognized by the linkage of the Y1 and the Z1.

Taking the crown worm wheel center O_w as the basis point, according to the structure and motion characteristics of the machine tool, the crown worm wheel motion in the dressing process is shown in Fig. 9. In Fig. 9 a), the

Fig. 9 The dressing motion diagram of the crown worm wheel



crown worm wheel center O_w is in the same line as the diamond wheel center O_d in the vertical direction. E is the distance between the eccentric O_s and the crown worm wheel center O_w . There is an offset distance e_t between the wheel swivel axis center O_A and the diamond wheel center O_d in the horizontal direction, and an offset distance e_z from the crown worm wheel center O_w in the vertical direction. The offset distance is constant and depends on the machine tool structure. Figure 9 b) shows the motion of the crown worm wheel on the machine tool during the dressing is decomposed, and the travel of each axis of the crown worm wheel from the reference point “0” to any point “i” is calculated.

The center of the crown worm wheel reaches the position of O_w' from O_{w0} , which requires A1 to drive the tool holder to rotate by an angle Δa_i . At the same time, the Y1 and Z1 respectively move the distances of Δy_i and Δz_i , and the center of the crown worm wheel reaches the O_{wi} . The motion of the three axes is completed simultaneously. The O_w' is a virtual point, and the center of the crown worm wheel does not pass through this point in the actual dressing process. The relationship between the travel of the A1, Y1, and Z1 and the travel of the B1 is shown in Eq. (14).

$$\begin{cases} \Delta a_i = \Delta b_i / N_s \\ \Delta y_i = (E + e_z) \tan(\Delta b_i / N_s) + e_t (1 - 1 / \cos(\Delta b_i / N_s)) \\ \Delta z_i = -e_t \tan(\Delta b_i / N_s) - (E + e_z) (1 - 1 / \cos(\Delta b_i / N_s)) \end{cases} \quad (14)$$

3.4 Forming dressing simulation

The rotation of the diamond wheel does not change the shape and position of the profile of the shaft section involved in dressing. The diamond wheel is equivalent to a slice always in contact with the crown worm wheel. The coordinate transformation of the machine motion calculates the dressed crown worm wheel profile. Figure 10 shows the equivalent slice of the formed diamond wheel, the curve equation of the diamond wheel is shown in Eq. (15).

$$\vec{r}_d = \begin{bmatrix} x_d \\ y_d \\ z_d \\ 1 \end{bmatrix} = \begin{bmatrix} -r_{bd} [\cos(\theta_{os} + \theta_d) + \theta_d \sin(\theta_{os} + \theta_d)] + r_{bd} + R_d \\ \pm r_{bd} [\sin(\theta_{os} + \theta_d) - \theta_d \cos(\theta_{os} + \theta_d)] \\ 0 \\ 1 \end{bmatrix} \quad (15)$$

where r_{bd} is the radius of the base circle of the diamond wheel, θ_d is an involute variable parameter, and R_d is the radius of the diamond wheel.

The crown worm wheel dressing motion coordinate system is based on the virtual center distance principle. The

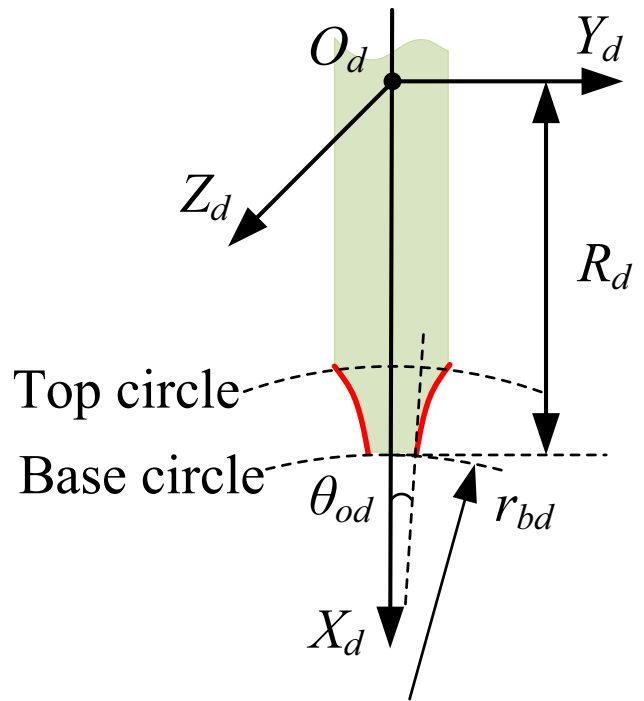


Fig. 10 The equivalent slice of diamond wheel

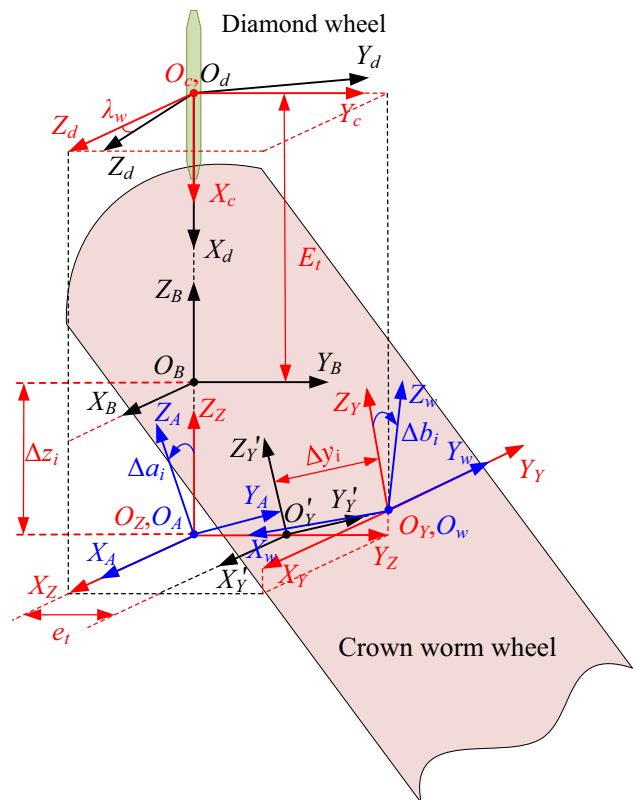


Fig. 11 The dressing motion coordinate systems of the crown worm wheel

coordinate system S_d is the moving coordinate system of the diamond wheel, S_C is the moving coordinate system of the C2, S_B is the fixed coordinate system of the machine tool bed, S_Z is the Z1 motion coordinate system, S_A is the A1 motion coordinate system, $S_{Y'}$ is the Y1 fixed coordinate system, S_Y is the Y1 motion coordinate system, S_w is the crown worm wheel motion coordinate system (Fig. 11).

The coordinate transformation from the diamond wheel to the crown worm wheel is shown in Eq. (16).

$$M_{wd}(\Delta b_i) = M_{wY}M_{YY'}M_{Y'A}M_{AZ}M_{ZB}M_{BC}M_{Cd} \tag{16}$$

where M_{wY} , $M_{YY'}$, $M_{Y'A}$, M_{AZ} , M_{ZB} , M_{BC} , and M_{CD} are

$$M_{Cd} = \begin{bmatrix} 1 & 0 & 0 & 0 \\ 0 & \cos\lambda_w & \sin\lambda_w & 0 \\ 0 & -\sin\lambda_w & \cos\lambda_w & 0 \\ 0 & 0 & 0 & 1 \end{bmatrix} M_{BC} = \begin{bmatrix} 0 & 0 & 1 & 0 \\ 0 & 1 & 0 & 0 \\ -1 & 0 & 0 & E_t \\ 0 & 0 & 0 & 1 \end{bmatrix} \tag{17}$$

$$M_{ZB} = \begin{bmatrix} 1 & 0 & 0 & 0 \\ 0 & 1 & 0 & 0 \\ 0 & 0 & 1 & \Delta z_i \\ 0 & 0 & 0 & 1 \end{bmatrix} M_{AZ} = \begin{bmatrix} 1 & 0 & 0 & 0 \\ 0 & \cos\Delta a_i & \sin\Delta a_i & 0 \\ 0 & -\sin\Delta a_i & \cos\Delta a_i & 0 \\ 0 & 0 & 0 & 1 \end{bmatrix} \tag{18}$$

$$M_{Y'A} = \begin{bmatrix} 1 & 0 & 0 & 0 \\ 0 & 1 & 0 & -e_t \cos\Delta a_i \\ 0 & 0 & 1 & e_t \sin\Delta a_i \\ 0 & 0 & 0 & 1 \end{bmatrix} M_{YY'} = \begin{bmatrix} 1 & 0 & 0 & 0 \\ 0 & 1 & 0 & -\Delta y_i \\ 0 & 0 & 1 & 0 \\ 0 & 0 & 0 & 1 \end{bmatrix} \tag{19}$$

$$M_{wY} = \begin{bmatrix} \cos\Delta b_i & 0 & \sin\Delta b_i & 0 \\ 0 & 1 & 0 & 0 \\ -\sin\Delta b_i & 0 & \cos\Delta b_i & 0 \\ 0 & 0 & 0 & 1 \end{bmatrix} \tag{20}$$

where $E_t = R_t + r_{bd} + E + e_z$, R_t is the radius of the diamond wheel, Δz_i is the travel of the Z1 in the dressing process, Δa_i is the rotation angle of the A1 in the dressing process, Δy_i is the travel of the Y1 in the dressing process, Δb_i is the rotation angle of the B1 in the dressing process.

There is only one independent motion parameter Δb_i in the dressing process of the crown worm wheel. Calculating the profile of the crown worm wheel after the dressing is shown in Eq. (21).

$$\vec{r}_{wg}(\theta_d, \Delta b_i) = M_{wd}(\Delta b_i)\vec{r}_d(\theta_d) \tag{21}$$

Taking the design parameters in Table 1 as an example, the numerical simulation of the dressing process is carried out. The results are shown in Fig. 12. Fig. a) is the numerical simulation profile, and Fig. b) is the theoretical profile. The overall profile of the two is consistent, which preliminarily proves that the numerical simulation is correct.

Eight helixes are evenly selected along the tooth height direction on both sides of the surface. The normal deviation between the numerical simulation surface and the theoretical surface is calculated along the helix. The results are shown in Fig. 13. The deviation value increases linearly from the middle of the crown worm wheel surface to both sides, and the deviation values of the left and right profiles are opposite. Still, the deviation values are below 5×10^{-6} mm, within the allowable error range. It is verified that the decomposition of the dressing movement based on the principle of virtual center distance is correct. The dressing movement of the crown worm wheel can be completed by linking the B1, A1, Y1, and Z1.

Table 1 Design parameters of face gear and crown worm wheel

Parameters	Value
Number of shaper cutter teeth N_s	32
Number of face gear teeth N_2	90
Number of crown worm wheel heads N_w	1
Module m /mm	4
Pressure angle α '°	20
Tooth top height coefficient h_a^*	1
Gap Coefficient c^*	0.25
Distance between shaper cutter and worm $E_{ws}(E)$ /mm	60
Number of pinion teeth N_1	30
The inner diameter of face gear R /mm	350
The outer diameter of face gear r /mm	394

Fig. 12 Dressing numerical simulation results of the crown worm wheel

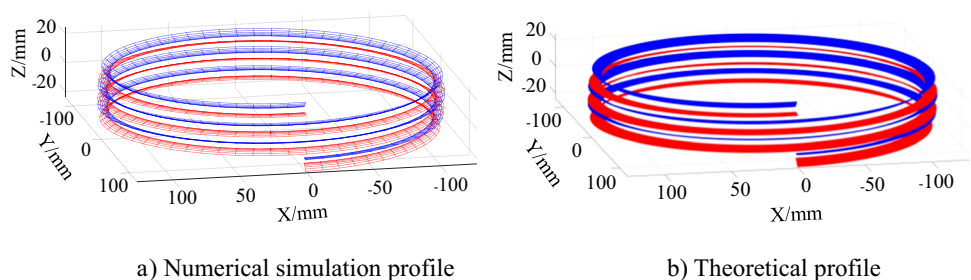


Fig. 13 The surface deviation between numerical simulation and theoretical calculation

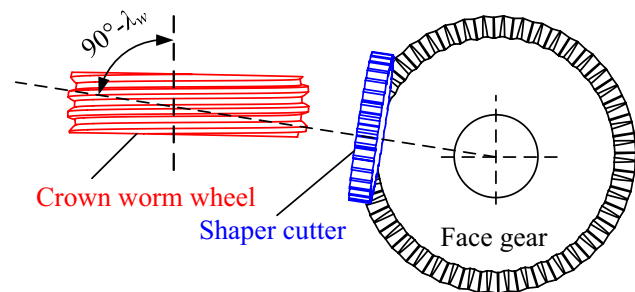
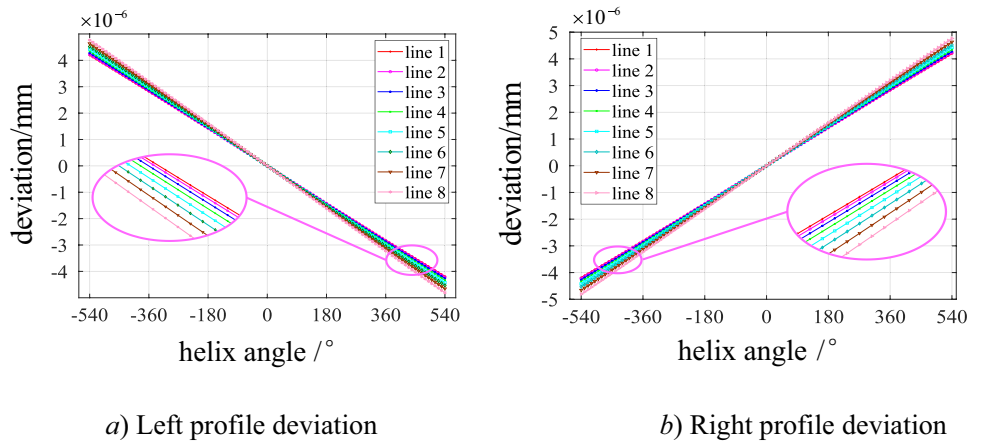


Fig. 14 The corresponding shaper of the worm without deflection

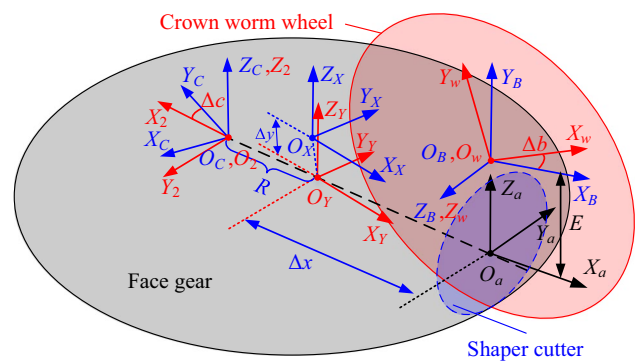


Fig. 16 The worm grinding motion coordinate systems

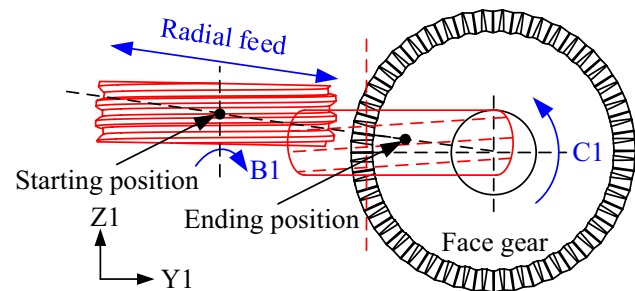


Fig. 15 Crown worm wheel grinding trajectory

4 Face gear grinding method

4.1 Grinding method

The general cylindrical gear grinding machine cannot realize the deflection of the crown worm wheel in the horizontal plane. The trajectory of the crown worm wheel is replanned when the crown worm wheel axis is parallel to the Y1 of the gear grinding machine [33]. Figure 14 shows the angle between the crown worm wheel axis and the shaper cutter axis is always $90^\circ - \lambda_w$. The teeth of the face gear are distributed in a ring shape on the end face, and the shaper cutter can still mesh with the face gear when it is in the position shown in the figure.

Figure 15 shows the motion of each axis and the trajectory of the crown worm wheel when the face gear is grinding. The crown worm wheel and the face gear are rotated proportionally according to Eq. (1) relationship through the B1 and C1. At the same time, through the linkage of the X1 and Y1, the crown worm wheel radial feed from the starting position shown in the figure to the ending position along the shaper cutter axis, completing a full grinding travel, and there is no principal error in motion geometry. The relationship between the radial feed motion of the X1 and Y1 is shown in Eq. (22).

$$\Delta y = \Delta x \tan \lambda_w \tag{22}$$

where Δx and Δy are the linkage travel of the X1 and Y1.

4.2 Grinding simulation

The face gear is expressed by the spiral surface equation of the crown worm wheel and the motion of the machine. The constant ratio rotation of the crown worm wheel, the face gear, and the linear feed of the crown worm wheel complete the grinding process. Therefore, the numerical simulation of the grinding process of the crown worm wheel is the two-parameter

envelope. The motion coordinate system of crown worm wheel grinding is shown in Fig. 16, S_w is the moving coordinate system of the crown worm wheel, S_B is rigidly attached to the crown worm wheel (B1), S_a is the auxiliary coordinate system, S_X and S_Y are the motion coordinate systems of X1 and Y1, S_C is the fixed coordinate system fixed of the workpiece (C1), S_2 is the moving coordinate system of face gear. Δb is the rotation angle of the B1, R is the minimum inner radius of the face gear, and Δc is the rotation angle of the C1. The face gear coordinate system is established at the same height as the shaper cutter axis corresponding to the crown worm wheel. The X of the S_C is co-line with the shaper cutter axis, which facilitates the comparison between the numerical simulation and the theoretical calculation.

When grinding the face gear on the gear grinding machine, the coordinate transformation matrix from crown worm wheel to face gear is shown in Eq. (23).

$$M_{2w}(\Delta b, \Delta x) = M_{2C}M_{CY}M_{Ya}M_{aB}M_{Bw} \tag{23}$$

where M_{2C} , M_{CY} , M_{Ya} , M_{aB} , and M_{Bw} are

$$M_{Bw} = \begin{bmatrix} \cos\Delta b & -\sin\Delta b & 0 & 0 \\ \sin\Delta b & \cos\Delta b & 0 & 0 \\ 0 & 0 & 1 & 0 \\ 0 & 0 & 0 & 1 \end{bmatrix} \quad M_{aB} = \begin{bmatrix} 1 & 0 & 0 & 0 \\ 0 & 0 & -1 & 0 \\ 0 & 1 & 0 & E \\ 0 & 0 & 0 & 1 \end{bmatrix} \tag{24}$$

$$M_{Ya} = \begin{bmatrix} 1 & 0 & 0 & \Delta x \\ 0 & 1 & 0 & -\Delta y \\ 0 & 0 & 1 & 0 \\ 0 & 0 & 0 & 1 \end{bmatrix} \quad M_{CY} = \begin{bmatrix} -\cos\lambda_w & \sin\lambda_w & 0 & -R \\ -\sin\lambda_w & \cos\lambda_w & 0 & 0 \\ 0 & 0 & 1 & 0 \\ 0 & 0 & 0 & 1 \end{bmatrix} \tag{25}$$

$$M_{2C} = \begin{bmatrix} \cos\Delta c & \sin\Delta c & 0 & 0 \\ -\sin\Delta c & \cos\Delta c & 0 & 0 \\ 0 & 0 & 1 & 0 \\ 0 & 0 & 0 & 1 \end{bmatrix} \tag{26}$$

The relationship between Δc and Δb is shown in Eq. (27).

$$\Delta c = \frac{N_w}{N_2} \cdot \Delta b \tag{27}$$

According to the coordinate transformation analysis, there are only two independent motion parameters, Δb and Δx , in the grinding process. The tooth surface of the face gear is shown in Eq. (28).

$$\vec{r}_2(\theta_s, \phi_s, \Delta b, \Delta x) = M_{2w}(\Delta b, \Delta x)\vec{r}_w(\theta_s, \phi_s) \tag{28}$$

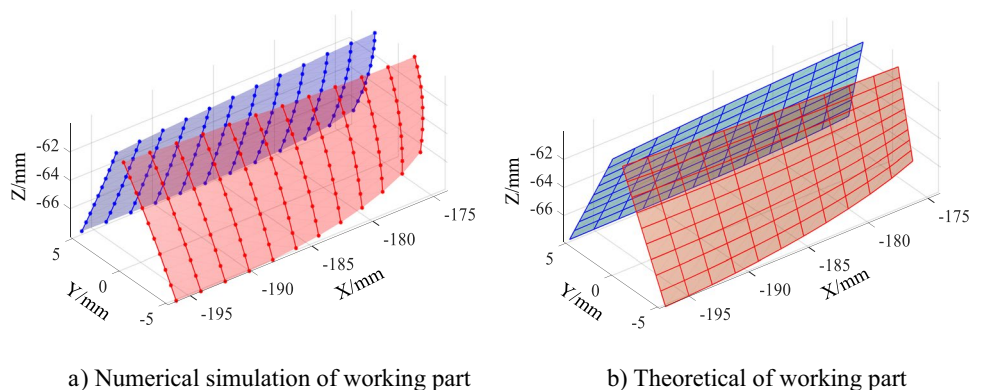
The face gear grinding meshing equation is shown in Eq. (29).

$$\begin{cases} f(\theta_s, \phi_s, \Delta b, \Delta x) = \left(\frac{\partial \vec{r}_2}{\partial \theta_s} \times \frac{\partial \vec{r}_2}{\partial \phi_s} \right) \cdot \frac{\partial \vec{r}_2}{\partial \Delta b} = 0 \\ g(\theta_s, \phi_s, \Delta b, \Delta x) = \left(\frac{\partial \vec{r}_2}{\partial \theta_s} \times \frac{\partial \vec{r}_2}{\partial \phi_s} \right) \cdot \frac{\partial \vec{r}_2}{\partial \Delta x} = 0 \end{cases} \tag{29}$$

where $\frac{\partial \vec{r}_2}{\partial \theta_s} \times \frac{\partial \vec{r}_2}{\partial \phi_s}$ is the normal vector of the instantaneous contact point and $\frac{\partial \vec{r}_2}{\partial \Delta b}$ is the relative velocity of the instantaneous contact point in the grinding process. $\frac{\partial \vec{r}_2}{\partial \Delta x}$ is the relative velocity of the instantaneous contact point when the crown worm wheel radial feed.

The tooth equations and meshing equations of the face gear are calculated, taking the design parameters shown in Table 1 as an example, using the meshing Eqs. (28) and (29) to eliminate the parameters ϕ_s and Δb and taking values for θ_s and Δx , a series of discrete points on the working part of the face gear are calculated. The results are shown in Fig. 17, where a) is the working part obtained from the double parameter envelope, and b) is the theoretical working part obtained from the single parameter envelope of the shaper cutter. The two profiles are the same, proving that the numerical simulation calculation is correct. The fillet part is enveloped by the crown worm wheel's outer edge, and the numerical simulation process does not independently analyze the crown worm wheel's outer edge.

Fig. 17 Worm grinding numerical simulation results of face gear



The theoretical tooth surface points corresponding to the discrete points of the numerical simulation tooth surface are calculated. The discrete points of the numerical simulation tooth surface are $s_i(x_i^{(s)}, y_i^{(s)}, z_i^{(s)})$, and the corresponding points of the theoretical tooth surface are $t_i(x_i^{(t)}, y_i^{(t)}, z_i^{(t)})$. Let $x_i^{(t)} = x_i^{(s)}$, $z_i^{(t)} = z_i^{(s)}$ be substituted into Eq. (7), and the corresponding $y_i^{(t)}$ is solved. The coordinates of the corresponding points on the theoretical tooth surface are obtained, and the normal unit vector \vec{n}_i of each point on the theoretical tooth surface is shown in Eq. (30).

$$\vec{n}_i = \frac{\frac{\partial \vec{r}_2}{\partial \theta_s} \times \frac{\partial \vec{r}_2}{\partial \phi_s}}{\left| \frac{\partial \vec{r}_2}{\partial \theta_s} \times \frac{\partial \vec{r}_2}{\partial \phi_s} \right|} \quad (30)$$

where \vec{r}_2 is the tooth surface equation of the face gear enveloped by the shaper cutter.

The normal deviation of the corresponding point is shown in Eq. (31).

$$d_i = (\vec{r}_{s_i} - \vec{r}_{t_i}) \cdot \vec{n}_i \quad (31)$$

where \vec{r}_{s_i} is the vector from the origin to the numerical tooth surface point, and \vec{r}_{t_i} is the vector from the origin to the theoretical tooth surface point.

The normal deviation between the numerical simulation tooth surface and the theoretical tooth surface is shown in Fig. 18. The left and right tooth surface deviations are both negative, and the variation trend is consistent. In the tooth profile direction, the tooth top deviation is slightly larger than the tooth root deviation, and the departure from tooth top to tooth root decreases somewhat. In the tooth width direction, the tooth surface deviation near the inner diameter is less than near the outer diameter. The tooth surface deviation from the inner diameter to the outer diameter decreases first and then increases. Overall, the variation of the numerical simulation tooth surface relative to the theoretical tooth surface is less than 5×10^{-5} mm, within the allowable error range. The numerical

simulation results prove the correct replanned crown worm wheel grinding trajectory.

5 Experiment

5.1 Tool misalignment error analysis

The outer edge of the crown worm wheel is circular, and its cross profile varies periodically along the arc. In practice, due to the installation error or machine error, the crown worm wheel is offset along the Y-axis during grinding, causing changes in the tooth shape of the face gear, so the crown worm wheel must be strictly aligned when grinding the face gear. The grinding wheel is offset e_y along the Y-axis during grinding, as shown in Fig. 19. The actual grinding trajectory of the crown worm wheel is shown as the blue line in the figure. The coordinate transformation relationship between S_w and S_B is shown in Fig. 20. The error matrix is introduced as

$$M_e = \begin{bmatrix} 1 & 0 & 0 & 0 \\ 0 & 1 & 0 & e_y \\ 0 & 0 & 1 & 0 \\ 0 & 0 & 0 & 1 \end{bmatrix} \quad (32)$$

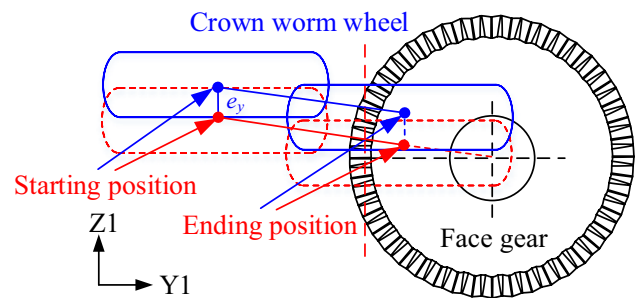
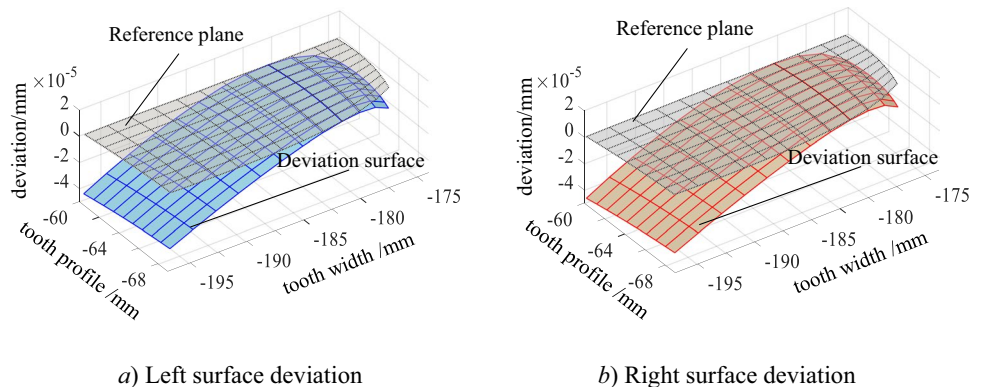


Fig. 19 Grinding trajectory of wheel misalignment

Fig. 18 Normal deviation of tooth surface between numerical simulation and theoretical calculation



a) Left surface deviation

b) Right surface deviation

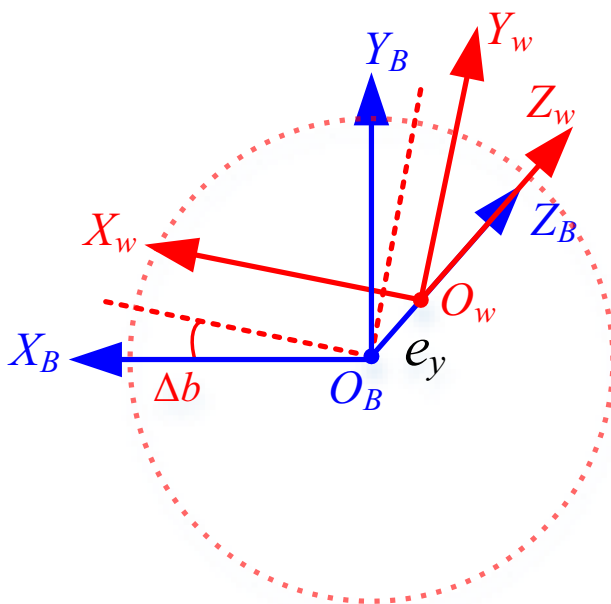


Fig. 20 Coordinate transformation relation of wheel misalignment

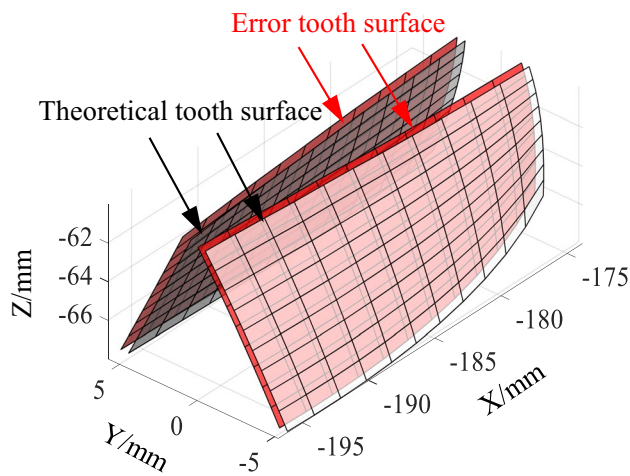


Fig. 21 Error surface and theoretical surface

The coordinate transformation matrix from crown worm wheel to face gear is shown in Eq. (33).

$$M_{2w}^{(e)}(\Delta b, \Delta x) = M_{2C}M_{CY}M_{Ya}M_{aB}M_{Bw}M_e \tag{33}$$

The tooth surface of the face gear is shown in Eq. (34).

$$\vec{r}_2^{(e)}(\theta, \beta, \Delta b, \Delta x) = M_{2w}^{(e)}(\Delta b, \Delta x)\vec{r}_w(\theta_s, \phi_s) \tag{34}$$

Taking Table 1 as the calculation example, set the wheel offset is 0.3 mm, the face gear tooth surface with wheel

misalignment is calculated, as shown in Fig. 21, and the tooth surface is offset in the Y-axis. The normal deviation of the calculated error tooth face from the theoretical tooth face is shown in Fig. 22, and the maximum deviation of the tooth face does not exceed 0.03 mm. In the tooth profile direction, the left and right tooth faces vary less from the root to the top of the tooth. In the tooth width direction, the deviation of the left tooth face varies linearly from positive to negative from the inner diameter to the outer diameter, while the right tooth face is the opposite.

The tooth surfaces on both sides of the face gear will be offset in the same direction when the crown worm wheel is offset on the Y-axis. Figure 23 shows that the face teeth will be in a "non-orthogonal" state with its axis. Therefore, additional rotation of the C-axis and offset of the feed trajectory are used for reverse adjustment to improve the tooth grinding accuracy.

5.2 Experimental verification

The YS7232 general cylindrical gear grinding machine was selected for crown worm wheel dressing and face gear grinding experiments. The effectiveness of the virtual center distance dressing method and diagonal feed continuous generation grinding method proposed in this study is verified. The face gear and crown worm wheel parameters are shown in Table 2. The machining process and results are shown in Fig. 24. The profile of the dressed crown worm wheel is consistent with the simulation results, and the tooth surface of the face gear after grinding is smooth.

The bevel gear measurement module of the Klingelnberg P26 gear measuring instrument was used to measure the machined face gear (as shown in Fig. 25). The machined tooth deviation is shown in Fig. 26. Analyzing the tooth error values of the machined face gear, the maximum error of the left tooth is $-6.0 \mu\text{m}$, and the maximum error of the right tooth is $5.8 \mu\text{m}$, both of which are within the error range allowed by the grade 5 accuracy. Considering the machining error of the grinding machine and the detection error of the measuring instrument, the tooth surface of the machined face gear is the same as the numerical simulation tooth surface, which verifies the effectiveness of the virtual center distance grinding wheel dressing method and the diagonal feed continuous spreading grinding method in this research, and the continuous generating grinding of face gears was realized on the general gear grinding machine.

6 Conclusion

A method of continuously generating grinding the face gears on a general cylindrical gear grinding machine is proposed to realize the precise manufacture of face gears.

Fig. 22 Normal deviation between error tooth surface and theoretical tooth surface

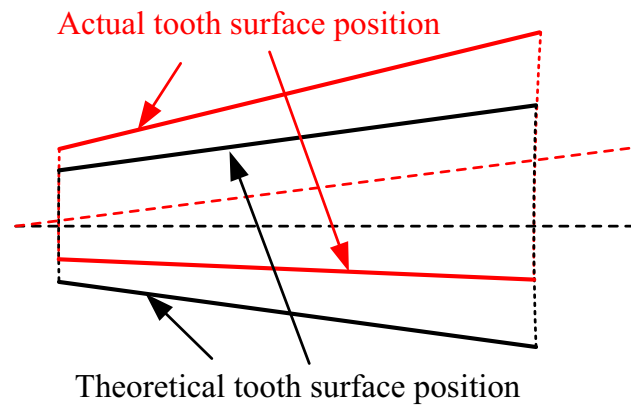
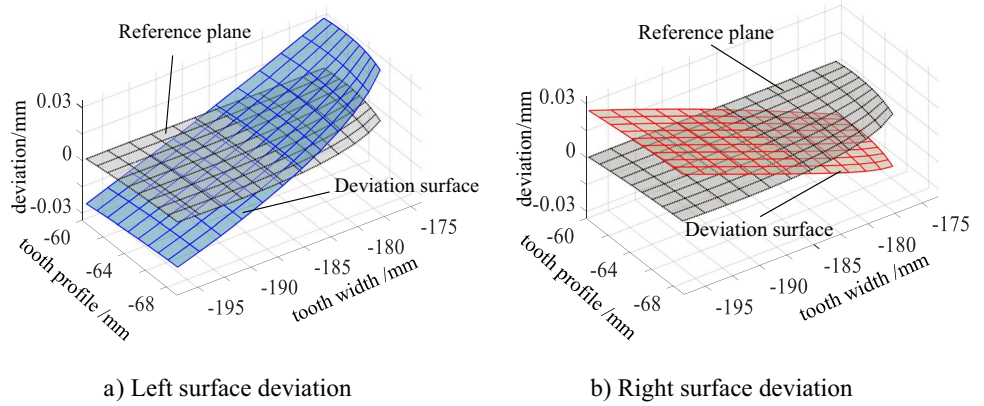


Fig. 23 Variation diagram of face gear tooth surface

1) The forming dressing method of the crown worm wheel with virtual center distance is proposed. This method solves the problem that the general cylindrical gear grinding machine cannot realize the large deflection of the diamond wheel when dressing the crown worm wheel. The deflection of the worm wheel replaces the deflection of the diamond wheel, and the dressing stroke is realized through the linkage of A1, Y1, Z1, and B1 four axes.

Table 2 Design parameters of face gear and crown worm wheel

Parameters	Value
Number of shaper cutter teeth N_s	23
Number of face gear teeth N_2	48
Number of crown worm wheel heads N_w	1
Module m/mm	3.9
Pressure angle $\alpha/^\circ$	25
Tooth top height coefficient h_a^*	1
Gap Coefficient c^*	0.25
Number of pinion teeth N_1	21
The inner diameter of face gear R/mm	180
The outer diameter of face gear r/mm	200

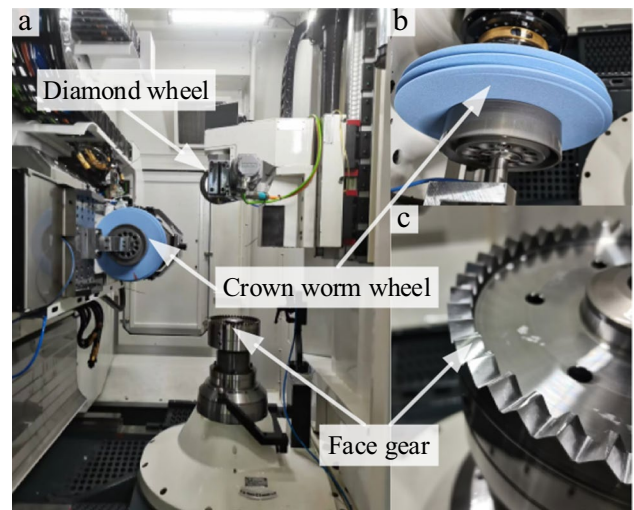


Fig. 24 (a) YS7232 gear grinding machine (b) Dressed crown worm wheel (c) Machined face gear

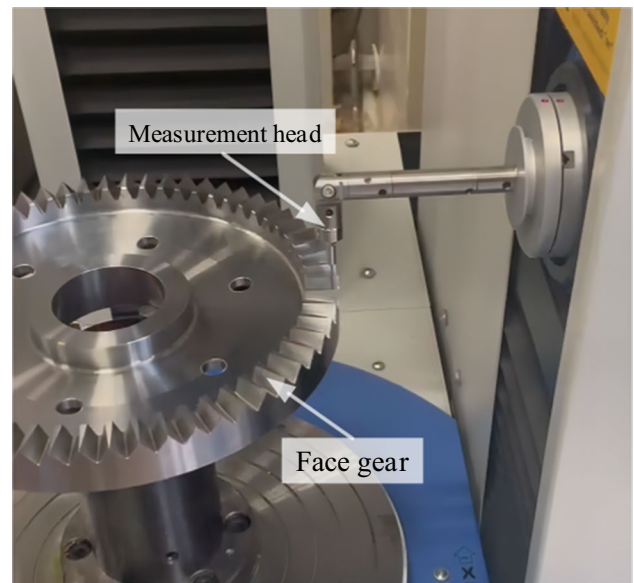


Fig. 25 Face gear measurement

Fig. 26 Tooth deviations of the face gear

	A	B	C	D	E	F	G	H	I		
	2.9	2.2	1.3	-0.3	-1.5	-2.4	-3.8	-6.0	-5.5	5	
	0.6	2.1	1.5	0.8	-1.9	-2.9	-3.1	-2.7	-5.1	4	
	2.7	1.5	1.2	-0.1	-1.2	-2.0	-2.2	-4.8	-3.3	3	
	1.0	2.4	1.1	0.9	0.3	-0.1	-2.9	-4.6	-6.0	2	
	2.5	1.9	1.2	1.4	0.3	-0.6	-2.0	-3.8	-2.3	1	
	LFI										
	Inside					Outside					
	RFI										
		-2.5	-2.8	2.3	0.6	-1.5	-0.9	4.2	2.5	4.3	1
		-0.5	-1.6	0.3	-2.9	-1.6	-0.8	1.1	3.1	4.1	2
		-0.2	-1.1	0.5	-0.7	0.6	-0.6	2.9	2.2	5.8	3
		-3.4	-1.4	-1.9	-1.6	0.4	-0.2	0.9	3.6	5.1	4
		-1.1	-1.8	-2.4	-2.2	-0.4	0.8	2.7	2.0	4.3	5
	A	B	C	D	E	F	G	H	I		

Unit: μm

- The radial feed trajectory of the crown worm wheel for grinding the face gear is planned. This method solves the problem that the general cylindrical gear grinding machine cannot realize the horizontal deflection of the worm wheel when grinding the face gear. This trajectory makes the crown worm wheel feed along the radial oblique line of the face gear through the linkage of X1 and Y1 axes.
- The tooth surface errors caused by the misalignment of the worm during grinding are analyzed. The numerical simulations and machining experiments are conducted for the crown worm wheel dressing and face gear grinding. The shape of the dressed crown worm wheel was consistent with the simulation results, the tooth surface of the face gear after continuous generating grinding was smooth, and the tooth surface error value is within the error range allowed for grade 5 accuracy.

The tooth surface configuration and precision grinding of face gears still need to be explored. Therefore, future work will modify the face gear tooth profile and study the continuous generating grinding processing method of complex modified face gears.

Funding We gratefully acknowledge the financial support of the Chongqing Natural Science Foundation (No. CSTB2022NSCQ-MSX0374), the China Postdoctoral Science Foundation (No.2021M700618) and the Chongqing Postdoctoral Research Program Special Grant (No.2021XMT005), the Innovative Research Group of Universities in Chongqing (No. CXQT21024).

Data availability The datasets used or analyzed during the current study are available from the corresponding author on reasonable request.

Declarations

Ethical approval Not applicable.

Consent to participate Not applicable.

Consent for publication Yes.

Competing interests The authors declare no competing interests.

References

- Litvin FL, Zhang Y, Wang J-C, Bossler RB Jr, Chen Y-JD (1992) Design and Geometry of Face-Gear Drives. *J Mech Des* 114:642–647
- Litvin F, Wang J, Bossler R, Chen Y, Heath G, Lewicki D (1994) Application of Face-Gear Drives in Helicopter Transmissions. *J Mech Des* 116:672–676
- Heath GF, Filler RR, Tan J (2002) Development of Face Gear Technology for Industrial and Aerospace Power Transmission. in: NASA/CR-2002–211320, Army. Research Laboratory ARL-CR-0485
- Wang J, Wang S, Ma C, Wang S, Dong J, Yang Y (2022) Identification of crucial geometric errors of face gear grinding machine based on geometric error-tooth surface normal error model considering worm dressing. *Mech Mach Theory* 176:105036
- Tang J, Yin F, Chen X (2013) The principle of profile modified face-gear grinding based on disk wheel. *Mech Mach Theory* 70:1–15
- Guo H, Peng X, Zhao N, Zhang S (2015) A CNC grinding method and envelope residual model for face gear. *Int J Adv Manuf Technol* 79:1689–1698
- Zhou R, Zhao N, Li W, Li R, Guo G, Guo H (2019) A grinding method of face gear mating with a conical spur involute pinion. *Mech Mach Theory* 141:226–244

8. Guo H, Zhao N, Zhang S (2013) Generation Simulation and Grinding Experiment of Face-Gear Based on Single Index Generating Method. In: Proceedings of the ASME 2013 International Design Engineering Technical Conferences and Computers and Information in Engineering Conference (IDETC/CIE 2013) pp. 1–7
9. Wang Y, Hou L, Lan Z, Zhang G (2016) Precision grinding technology for complex surface of aero face-gear. *Int J Adv Manuf Technol* 86:1263–1272
10. Wang Y, Liu Y, Chu X, He Y, Zhang W (2017) Calculation model for surface roughness of face gears by disc wheel grinding. *Int J Mach Tools Manuf* 123:76–88
11. Wang Y, Lan Z, Hou L, Zhao H, Zhong Y (2015) A precision generating grinding method for face gear using CBN wheel. *Int J Adv Manuf Technol* 79:1839–1848
12. Litvin FL, Fuentes A, Zanzi C, Pontiggia M, Handschuh RF (2002) Face-gear drive with spur involute pinion: geometry, generation by a worm, stress analysis. *Comput Methods Appl Mech Eng* 191:2785–2813
13. Litvin FL, Gonzalez-Perez I, Fuentes A, Vecchiato D, Hansen BD, Binney D (2005) Design, generation and stress analysis of face-gear drive with helical pinion. *Comput Methods Appl Mech Eng* 194:3870–3901
14. Cui W, Tang J (2017) New method for calculating face gear tooth surface involving worm wheel installation errors. *J Cent South Univ* 24:1767–1778
15. Shi X, Zhou Y, Zhang W, Tang J (2019) A new worm grinding method of face gears based on the optimization of dressing wheel profile. *Forsch Ingenieurwes* 83:751–757
16. Tang J, Cui W, Zhou H, Yin F (2016) Integrity of grinding face-gear with worm wheel. *J Cent South Univ* 23:77–85
17. Zhou Y, Tang J, Zhou H, Yin F (2016) Multistep Method for Grinding Face-Gear by Worm. *J Manuf Sci Eng* 138:071013
18. Wang S, Zhou Y, Tang J, Tang K, Li Z (2022) Digital tooth contact analysis of face gear drives with an accurate measurement model of face gear tooth surface inspected by CMMs. *Mech Mach Theory* 167:104498
19. Tang Z, Zhou Y, Wang S, Zhu J, Tang J (2022) An innovative geometric error compensation of the multi-axis CNC machine tools with non-rotary cutters to the accurate worm grinding of spur face gears. *Mech Mach Theory* 169:104664
20. Zhou Y, Tang Z, Shi X, Tang J, Li Z (2022) Efficient and accurate worm grinding of spur face gears according to an advanced geometrical analysis and a closed-loop manufacturing process. *J Cent South Univ* 29:1–13
21. Guo H, Zhang S, Wu T, Zhao N (2021) An approximate design method of grinding worm with variable meshing angle and grinding experiments of face gear. *Mech Mach Theory* 166:104461
22. Tang J, Yang X (2016) Research on manufacturing method of planing for spur face-gear with 4-axis CNC planer. *Int J Adv Manuf Technol* 82:847–858
23. Guo H, Gonzalez-Perez I, Fuentes-Aznar A (2019) Computerized generation and meshing simulation of face gear drives manufactured by circular cutters. *Mech Mach Theory* 133:44–63
24. Guo H, Ma T, Zhang S, Zhao N, Fuentes-Aznar A (2022) Computerized generation and surface deviation correction of face gear drives generated by skiving. *Mech Mach Theory* 173:104839
25. Chu X, Wang Y, Du S, Huang Y, Su G, Liu D, Zang L (2020) An efficient generation grinding method for spur face gear along contact trace using disk CBN wheel. *Int J Adv Manuf Technol* 110:1179–1187
26. Zschippang HA, Weikert S, Küçük KA, Wegener K (2019) Face-gear drive: Geometry generation and tooth contact analysis. *Mech Mach Theory* 142:103576
27. Wang Y, Su G, Chu X, Huang YES, Zhang W, Liu Y (2021) A finishing method for the continuous generation of spur face gears with shaving cutters. *Int J Mech Sci* 190:106020
28. Zhang W, Wei X, Guo X, Tan R, Wang Y (2022) A novel continuous indexing method for face-hobbed hypoid gear tooth grinding. *Mech Mach Theory* 173:104826
29. Yang X, Tang J (2014) Research on manufacturing method of CNC plunge milling for spur face-gear. *J Mater Process Technol* 214:3013–3019
30. Zhou Y, Wu Y, Wang L, Tang J, Ouyang H (2019) A new closed-form calculation of envelope surface for modeling face gears. *Mech Mach Theory* 137:211–226
31. Litvin FL, Fuentes A (2004) *Gear Geometry and Applied Theory*, 2nd edn. Cambridge University Press, Cambridge
32. Chen Y, Zhang G, Chen B (2012) Study on the Principle of Internal Gear Manufacturing Based on Crown Worm Driving. *J Mech Eng* 48:18–24
33. Peng X, Zhao P, Hu X, Xu L, Kan C (2021) Grinding method for face gear based on four-axis CNC machine tool. *J Aerosp Power* 36:1113–1120

Publisher's note Springer Nature remains neutral with regard to jurisdictional claims in published maps and institutional affiliations.

Springer Nature or its licensor (e.g. a society or other partner) holds exclusive rights to this article under a publishing agreement with the author(s) or other rightsholder(s); author self-archiving of the accepted manuscript version of this article is solely governed by the terms of such publishing agreement and applicable law.